Supporting Information

Intrinsic oxygen vacancy synergistic Co site rapidly regulates electron transfer for efficient activation of peroxymonosulfate

Yingdi Zhang[1], Yunsheng Shang[1], Weiting Zhao, Qianxia Wang, Jin Yang, Yingqiu Gu[*], Guohai Yang, Lu-Lu Qu[*]

School of Chemistry & Materials Science, Jiangsu Normal University, Xuzhou, 221116, China

[*] Corresponding E-mail: guyingqiu@jsnu.edu.cn; luluqu@jsnu.edu.cn

[1] Yingdi Zhang and Yunsheng Shang contributed equally to this work.

Text S1：

Materials and reagents

Poly (ethylene glycol)-block-poly (propylene glycol)-block-poly (ethylene glycol) (PEG-PPG-PEG, P123), Mav = 5800 was purchased from Sigma Odrich (Shanghai) Trading Co., Ltd. $Al(NO)_3·9H_2O$ (AR), $Co(NO)_2·6H_2O$ (AR), citric acid monohydrate ($C_6H_8O_7·H_2O$, GR) was purchased from National Pharmaceutical Group Chemical Reagents Co., Ltd. Sodium hydroxide (NaOH, AR), methanol (CH_3OH, MeOH, ≥ 99.5%), isopropyl alcohol (C_3H_8O, IPA, ≥ 99.5%), furfuryl alcohol ($C_5H_6O_2$, FFA, AR), *p*-benzoquinone ($C_6H_4O_2$, *p*-BQ, 99%), potassium peroxomonosulfate ($H_3K_5O_{18}S_4$, PMS), $NaHCO_3$, NaCl, Na_2HPO_4, NaH_2PO_4, potassium thiocyanate (KSCN, AR), humic acid (HA, ≥ 90%), rhodamine 6G (R6G), malachite green (MG), methylene blue (MB), methyl orange (MO, 96%), eosin Y (EY), *p*-nitrophenol ($C_6H_5NO_3$, PNP), *o*-aminophenol (OAP), benzidine ($C_{12}H_{12}N_2$), bisphenol A (BPA, > 99.0%), tetracycline hydrochloride, oxytetracycline hydrochloride, trimethoprim and enrofloxacin were purchased from Aladdin Biochemical Technology Co., Ltd. (Shanghai, China). The actual wastewater comes from the secondary wastewater of two kinds of dye production produced by Jiangsu Noen Crop Science Co., Ltd. (Xuzhou, China)

Characterization

Transmission electron microscopy (TEM) images were acquired using an FEI Tecnai G2 F30 instrument operated at 300 KV. The catalyst was performed by energy dispersive X-ray spectroscopy (EDX) mapping in scanning transmission electron microscopy mode on the same machine. Scanning electron microscopy (SEM) images were captured with a Hitachi SU8010 field emission scanning microscope at an accelerating voltage of 5 KV. The powder X-ray diffraction (XRD) patterns were recorded on the D8 Advance diffractometer in Bruker, Germany, and the crystal structure was characterized by Cu Kα radiation (λ = 1.54178 Å). X-ray photoelectron spectroscopy (XPS) measurements were conducted on a Thermo Scientific Escalab 250Xi spectrometer (USA, Thermoelectric) with monochromatic Al Kα radiation ($h\upsilon$ = 1486.6 eV) at 150 W power and 650 μm beam spot size. The charge correction uses C 1s = 284.8 eV to correct the binding energy (BE). Nitrogen adsorption-desorption isotherms were performed on an Autosorb-IQ2-VP nitrogen adsorption-desorption instrument (Quantachrome, USA) at 77 K after degassing under vacuum at 120°C for 6 h. Ultraviolet-visible (UV-Vis) spectroscopy was performed using the NanoDrop 2000C spectrophotometer (Thermo Scientific, USA). Raman spectra were collected using a XploRA PLUS confocal microscope equipped with a laser wavelength of 532 nm (HORIBA, France).

Synthesis and formation mechanism of CACNs catalyst

A series of catalysts with different cobalt molar fractions were synthesized via an evaporation-induced self-assembly method. Specifically, 2.0 g of polymer surfactant P123 was dissolved in 40 mL of anhydrous ethanol under magnetic stirring at room temperature until it was completely dissolved. Subsequently, 1.68 g of citric acid and a certain proportion of $Al(NO_3)_3·9H_2O$ and $Co(NO_3)_2·6H_2O$ were added respectively. The total molar quantity of metal nitrates was fixed at 40 mmol, while the Co/Al molar ratio was systematically varied. The above mixture was stirred for 5 h at room temperature and then transferred to an oven. The solvent was evaporated at 60 °C and completely dried after 48 h. Subsequently, the dried precursor was calcined in a tube furnace under flowing N_2 atmosphere, with a temperature ramp from room temperature to 400 °C (heating rate of 1 °C min^{-1}), followed by a 6 h dwell at the target temperature. The resulting black solid was treated with 200 mL of 2.5 mol L^{-1} NaOH solution under at least 12 h of stirring at room temperature. The product was then rinsed several times with deionized water until neutrality to remove excess NaOH and dried overnight at 60 °C. The final catalysts were labeled as XCACNs, where X denotes the nominal cobalt molar percentage (at.%) in the precursor.

The polymer surfactant P123, pH-regulating agent citric acid, and metal nitrate precursors were dissolved in anhydrous ethanol, respectively. Due to the unique amphiphilic properties of the surfactant, the copolymer P123 molecules spontaneously assembles into bimolecular layers in the solution. The hydrophilic head groups (ethylene oxide) generate electrostatic repulsion, attracting metal cations (Al^{3+} and Co^{2+}) into the ethylene oxide-rich domains to reduce the electrostatic repulsion to balance the negative surface charge. Coordination between nitrate ions (NO_3^-) and metal cations can disrupt the assembly balance of the organic-inorganic interface. However, carboxyl groups from citric acid serve as effective chelating agents for Al^{3+} and Co^{2+}. During the whole solvent evaporation process, carboxyl groups competes with NO_3^- and coordinate with metal ions, thereby stabilizing the metal ions at the organic-inorganic interface and preserving the structure. Upon high-temperature carbonization under N_2 atmosphere, the organic molecular layers are converted into a layered carbon framework. Subsequent treatment with NaOH solution removes a substantial portion of aluminum, exfoliating the original dense layered structure into carbon nanosheets embedded with residual Al and Co species.

CACNs Catalytic performance evaluation

The catalytic performance of the synthesized Fenton-like catalysts was primarily evaluated through R6G degradation at room temperature. In a typical experiment, 2 mg of catalyst was dispersed in 50 mL of R6G solution (10 mg L^{-1}, pH = 7.0) and magnetically stirred for 30 min to establish adsorption-desorption equilibrium. UV-vis spectroscopy was employed to quantify R6G concentrations before and after adsorption. Subsequently, 0.2 mM PMS was added to the reaction solution to initiate the catalytic degradation experiment. At a predetermined time interval of 2 min, liquid samples (1 mL) were collected, rapidly filtered through 0.22 μm polyethersulfone membranes, and then analyzed via UV-vis spectroscopy to monitor R6G concentration decay. In addition, catalytic activity was further assessed by degrading recalcitrant organic pollutants including MG, MB, MO, EY, PNP, OAP, benzidine, bisphenol A, tetracycline, oxytetracycline, trimethoprim and enrofloxacin. In order to evaluate the contribution of active species to the degradation of pollutants, we used MeOH, IPA, FFA and *p*-BQ as chemical scavengers for quenching experiments. The inhibition rate was calculated based on the removal rate of R6G.

Reaction kinetics for pollutant degradation were analyzed using Equation (1):

$$\ln(\frac{C_t}{C_0}) = -K_{obs} \times t \qquad (1)$$

Here, C_t and C_0 represent the pollutant concentrations at reaction time (t) and the initial time (t_0), respectively, while K_{obs} denotes the first-order kinetic constant (min^{-1}).

Long-term continuous degradation experiments were carried out in a packed bed reaction column. CACNs catalyst was uniformly dispersed in an ethanol-water mixture, then loaded onto the surface of PVDF base membrane via vacuum filtration, followed by vacuum drying at room temperature to obtain the composite membrane. The catalytic membrane was fixed in the reactor generating unit and sealed with a rubber belt to prevent water leakage. Subsequently, the Yuquan River water was sampled and spiked with R6G (10 mg L^{-1}) as a model organic contaminant for removal assessment. The reactant solution containing R6G (10 mg L^{-1}) and PMS (0.2 mM) was pumped into the reaction column at an inlet flow rate of 10 mL min^{-1} from the top inlet. Catalytic performance was assessed over 300 min of continuous operation. (The dimensions of the reactor: the height of the upper tube is 15 cm, the height of the lower tube is 5 cm, the inner diameter of the tubes is 4 cm, and the pore diameter of the water inlet and outlet is 4 mm.)

EPR measurement

At room temperature, spin-trapped EPR signals were detected in different air-saturated methanol/water dispersions of the corresponding samples. For $\cdot OH/SO_4^{\bullet-}$ detection in the CACNs/PMS/pollutant system: 2 mg catalyst and 5 mg PMS were added to 50 mL of aqueous solution. After 10 min reaction, 100 μL of reaction solution was added to 100 μL of DMPO solution with a concentration of 100 mM. After mixing, the sample was sealed with a capillary, and then put into the sample tube and immediately analyzed by EPR. 50 μL reaction solution was mixed with 100 μL DMPO methanol solution (100 mM), vortexed for 3 min, and injected into capillaries for measurement of $O_2^{\bullet-}$. Then, 100 μL TEMP solution (100 mM) was added to 100 μL reaction solution to detect $^1O_2$, and the suspension was impacted for 3 min, and then pulled into the capillary for detection. The DMPO spin-trapped EPR spectra of $\cdot OH/SO_4^{\bullet-}$ or $O_2^{\bullet-}$ in the catalyst/PMS system were tested using the same process except that the R6G solution was replaced with pure water or methanol. Oxygen vacancy characterization was performed by directly loading 10 mg catalyst powder into EPR sample tubes for analysis.

Theoretical calculation

All the DFT calculations were conducted based on the Vienna Ab-inito Simulation Package (VASP)[28, 29]. The exchange-correlation effects were described by the Perdew-Burke-Ernzerhof (PBE) functional within the generalized gradient approximation (GGA) method[30, 31]. The core-valence interactions were accounted by the projected augmented wave (PAW) method[32]. The energy cutoff for plane wave expansions was set to 400 eV, and the 1 × 1 × 1 Monkhorst-Pack grid k-points were selected to sample the Brillouin zone integration. The structural optimization was completed for energy and force convergence set at 1.0×10^{-4} eV and 0.05 eV $Å^{-1}$, respectively. Grimme's DFT-D3 methodology[33] was used to describe the dispersion interactions.

The adsorption energies (E_{ads}) of PMS are calculated by

$$E_{\mathrm{ads}} = E_{\mathrm{*PMS}} - E_{\mathrm{PMS}} - E_{\mathrm{Sub}} \qquad (2)$$

where E_{PMS} and $E_{\mathrm{*PMS}}$ represent the energies before and after the adsorption of PMS on the substrates, respectively. E_{sub} is the energy of LDH and Co_3O_4 surfaces.

The Gibbs free energy change (ΔG) of each step is calculated using the following formula:

$$\Delta G = \Delta E + \Delta ZPE - T\Delta S \qquad (3)$$

where ΔE is the electronic energy difference directly obtained from DFT calculations, ΔZPE is the zero point energy difference, T is the room temperature (298.15 K) and ΔS is the entropy change.

ZPE could be obtained after frequency calculation by[33]:

$$\mathrm{ZPE} = \frac{1}{2}\sum \boldsymbol{hvi} \qquad (4)$$

And the TS values of adsorbed species are calculated according to the vibrational frequencies[34]:

$$\mathbf{TS} = \boldsymbol{k_B T}\left[\sum_k \ln\left(\frac{1}{1-e^{-hv/k_B T}}\right) + \sum_k \frac{hv}{k_B T}\frac{1}{(e^{hv/k_B T}-1)} + 1\right] \qquad (5)$$

Text S2:

The effects of experimental parameters such as PMS dosage, R6G concentration and catalyst dosage were discussed, as shown in Figure S8. When the concentration of PMS was 0 ~ 0.2 mM, the removal efficiency of R6G was significantly improved, while the removal efficiency of R6G was not obvious when the concentration of PMS was 0.2 ~ 0.4 mM (Figure S8A). Therefore, from the perspective of the rational use of oxidants, the PMS concentration used in our experiment was 0.2 mM. The increase of R6G concentration significantly reduced the removal efficiency of CACNs/PMS system (Figure S8B), because the oxidant in the solution was determined and the number of free radicals produced in the system was limited. Therefore, the removal efficiency of high concentration of R6G was low, and the concentration of R6G used in our experiment was 10 mg L^{-1}. As the amount of catalyst increases from 0 to 4 mg, the degradation of R6G will be significantly enhanced (Figure S8C). However, the use of excessive catalysts may lead to problems such as excessive leakage of metal ions. Therefore, the catalyst concentration in the CACNs/PMS system is 2 mg.

Text S3:

In this catalytic system, •OH and $SO_4^{\bullet-}$ with high oxidation potential are the core driving force for pollutant degradation, and their sufficient generation can effectively counteract the quenching effect of real water matrix. As a non-radical ROS, $^1O_2$ is hardly interfered by quenching from common anions in water, which can compensate for the oxidation capacity loss of radical species and avoid the defect of high susceptibility to interference from a single oxidation pathway. The synergism of the two constructs a dual-pathway degradation system with strong anti-interference ability, thus maintaining stable and high degradation efficiency in real water samples.

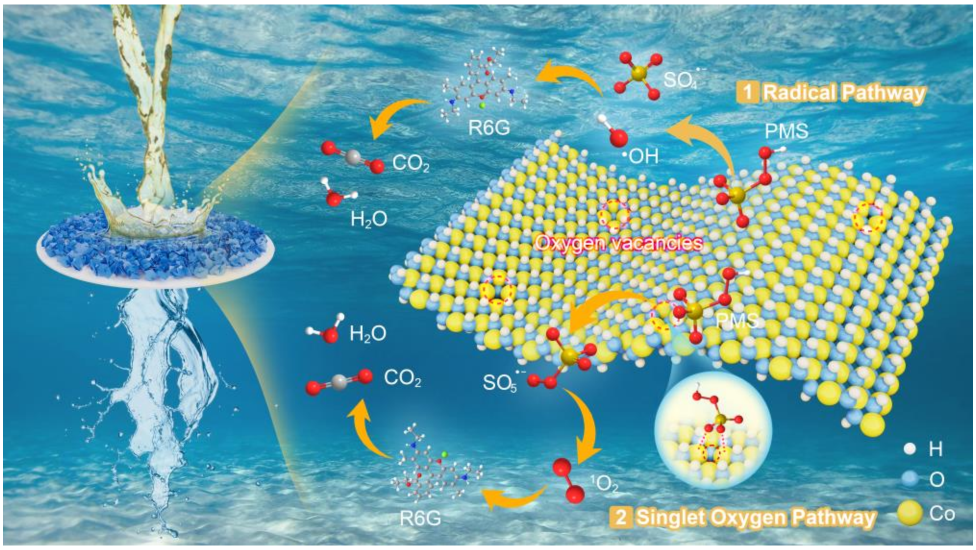

Figure S1. Mechanism diagram of pollutant degradation induced by CACNs activated PMS.

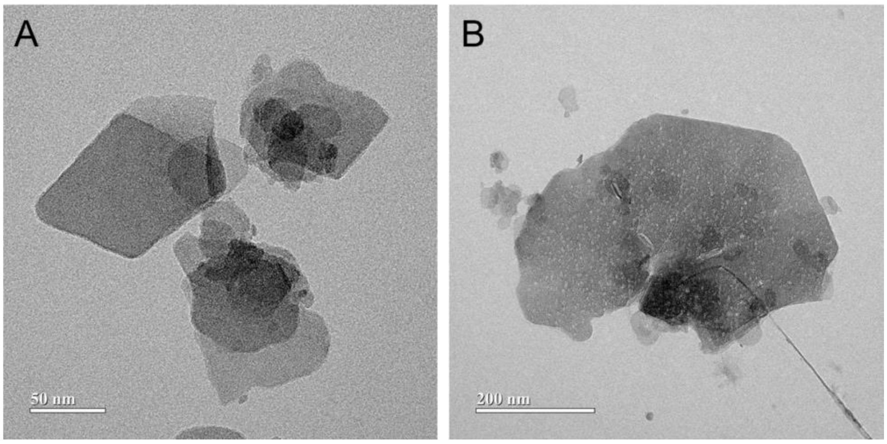

Figure S2. TEM images of CACNs.

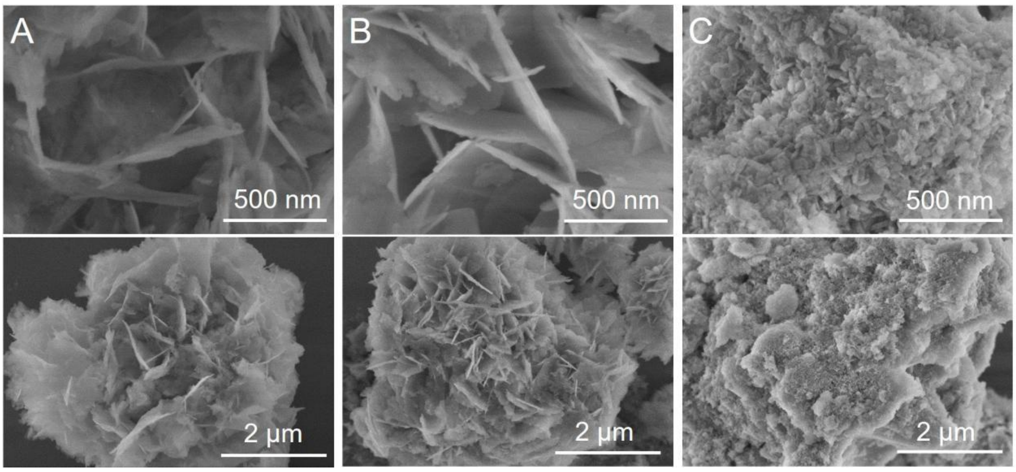

Figure S3. SEM images of (A) 15, (B) 30, (C) 50CACNs.

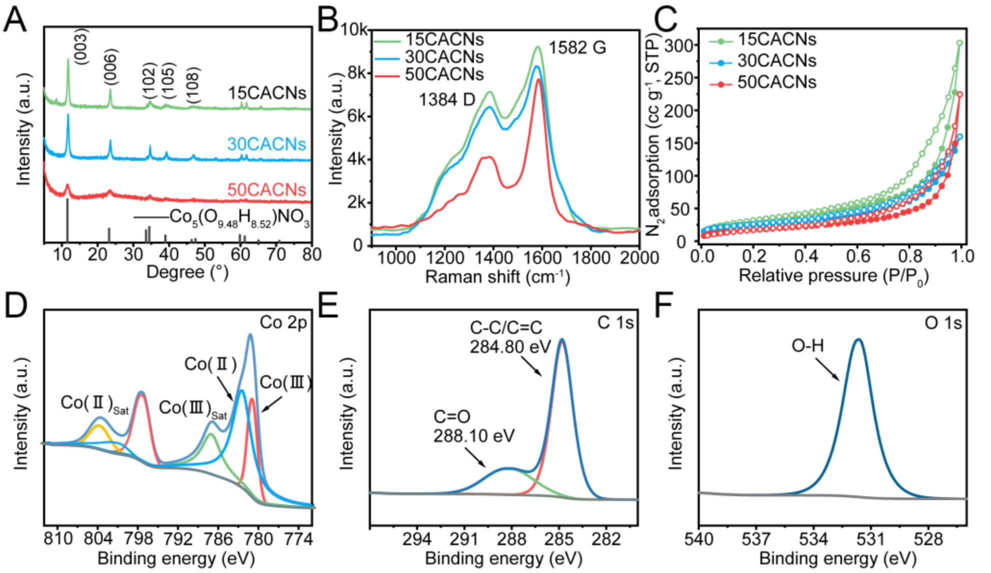

Figure S4. (A) XRD, (B) Raman spectra and (C) N_2 adsorption-desorption curves of CACNs. (D) Co 2p, (E) C 1s and (F) O 1s XPS spectra of CACNs.

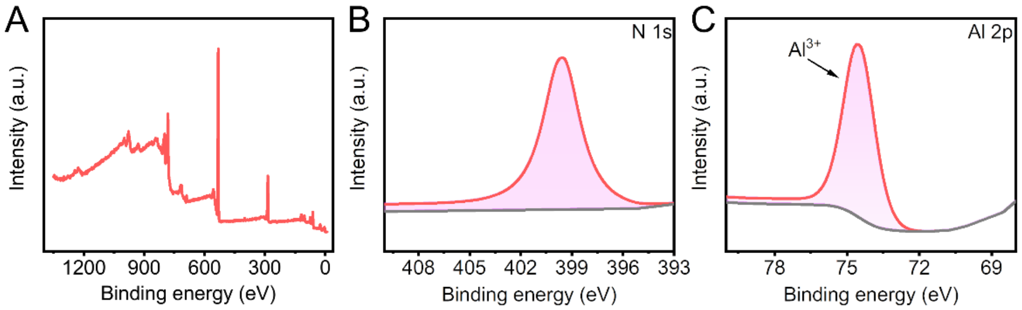

Figure S5. XPS spectra of CACNs: (A) Survey, (B) N 1s, and (C) Al 2p.

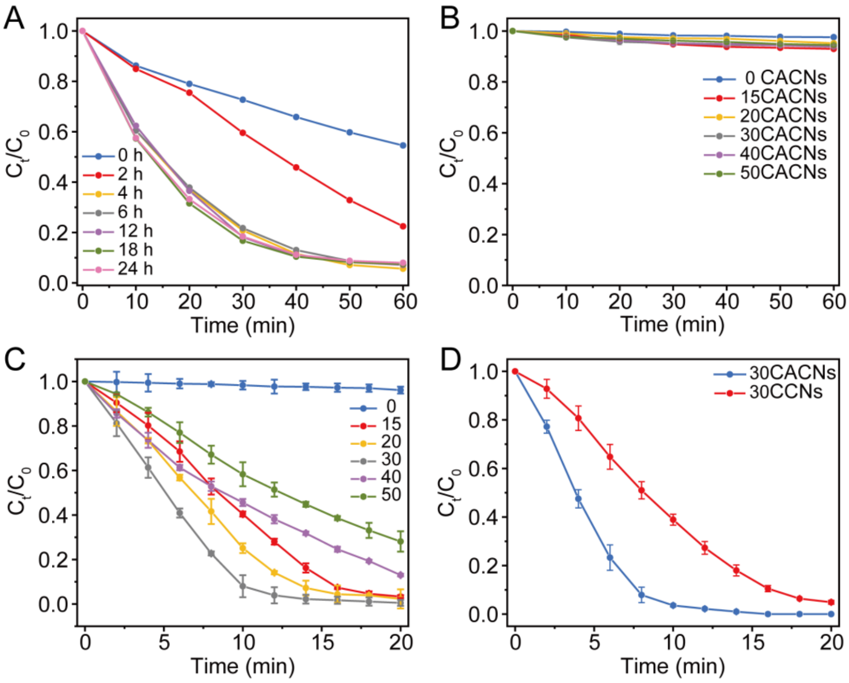

Figure S6. (A) The effect of CACNs/PMS system with different time of alkali stripping on the degradation performance of R6G. (B) Adsorption and (C) degradation performance of XCACNs on R6G under different Co loading conditions. (D) Removal efficiency of R6G degradation by CACNs in the presence or absence of Al.

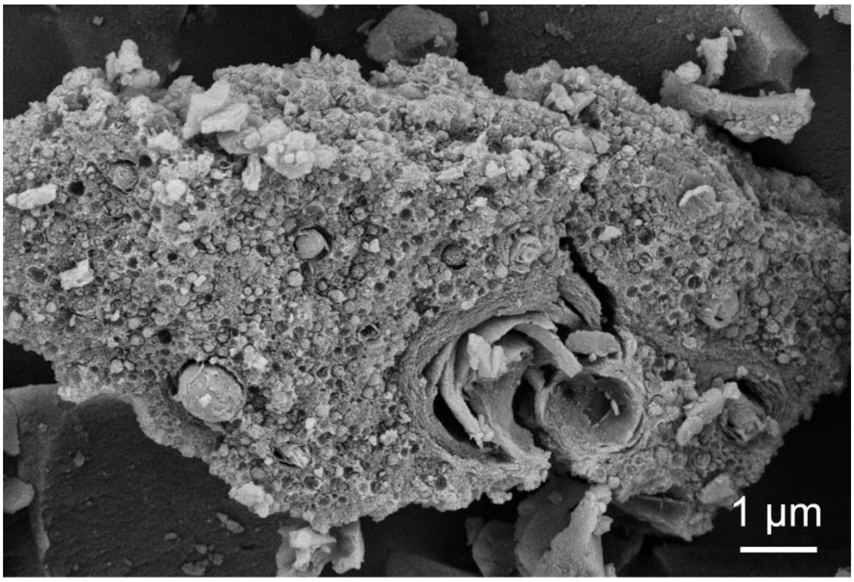

Figure S7. SEM of CACNs without alkali treatment.

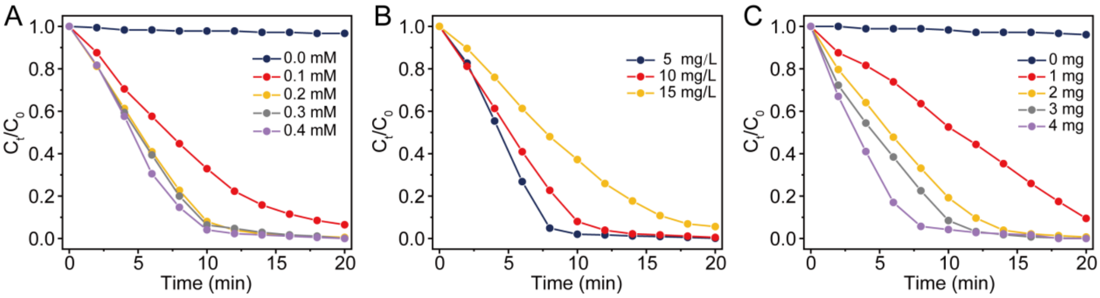

Figure S8. Degradation of R6G in CACNs/PMS system under different conditions: (A) PMS dosage, (B) R6G concentration, (C) catalyst dosage.

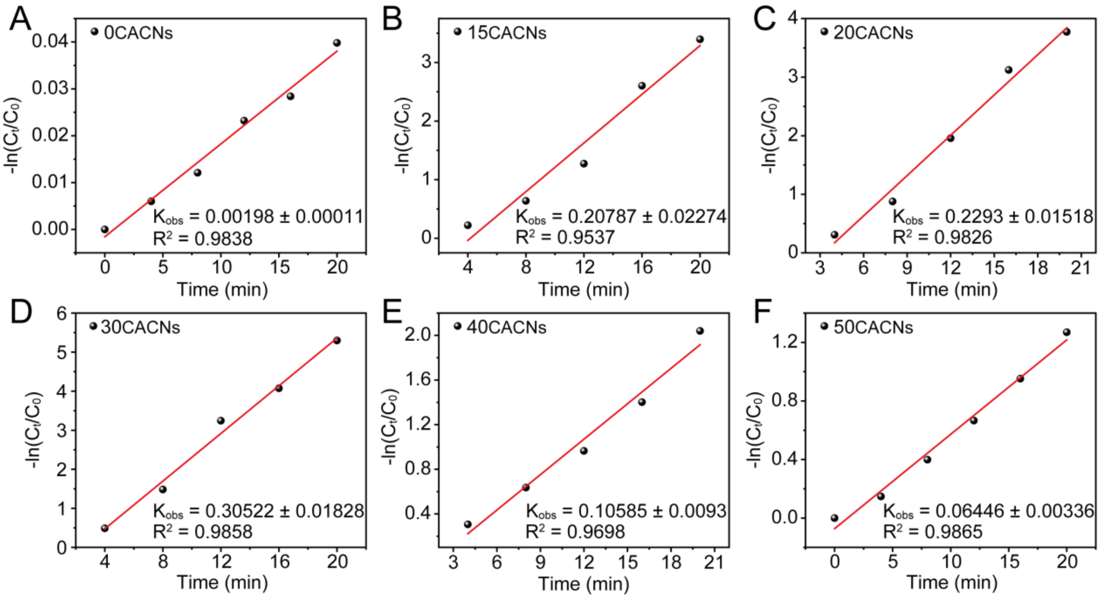

Figure S9. Time diagram of -ln(C_t/C_0) and CACNs.

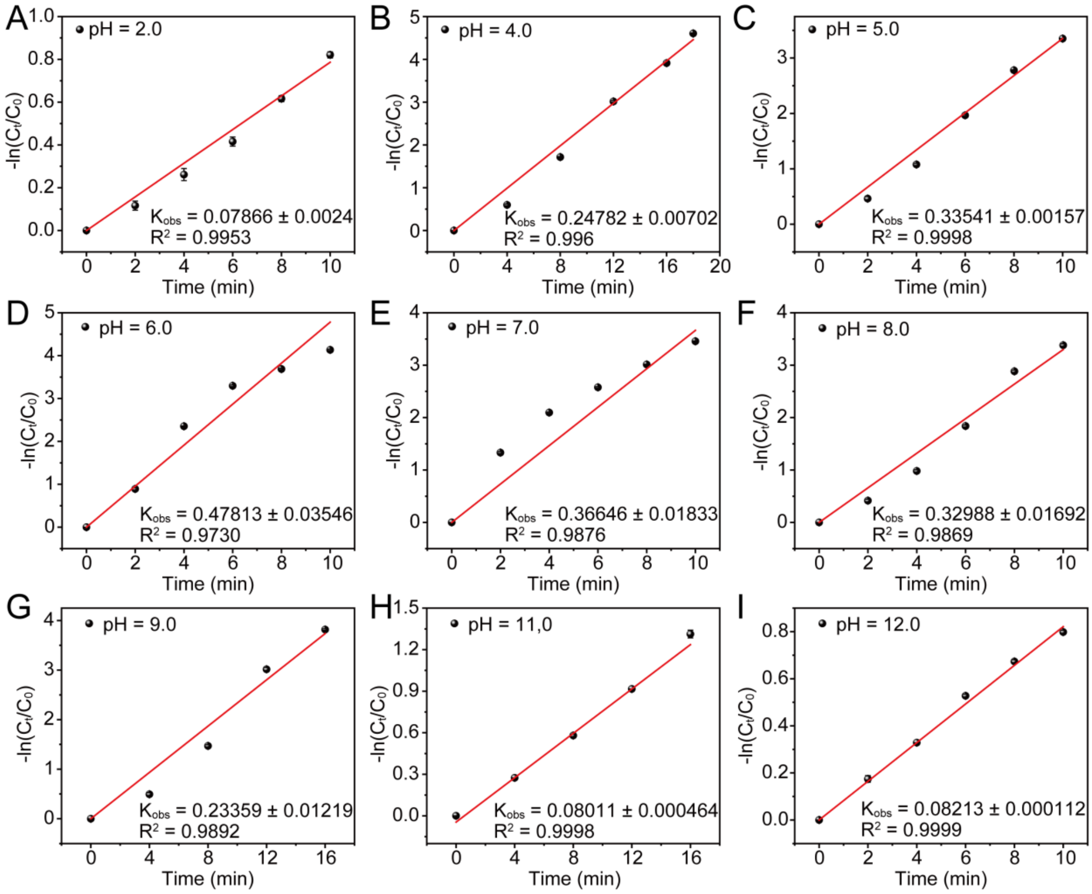

Figure S10. The first-order rate constants corresponding to different pH values in the CACNs/PMS system.

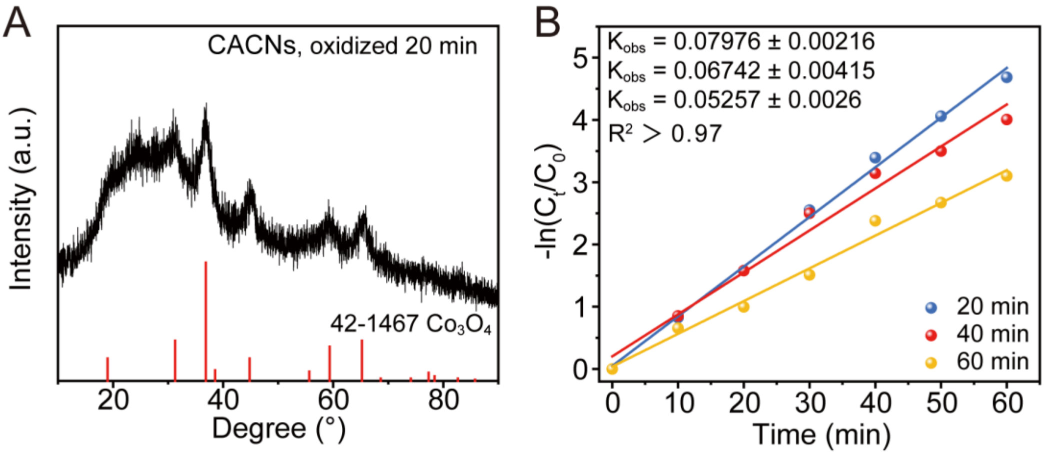

Figure S11. (A) The corresponding XRD of CACNs after oxidation for 20 min. (B) The corresponding first-order rate constants at different oxidation time.

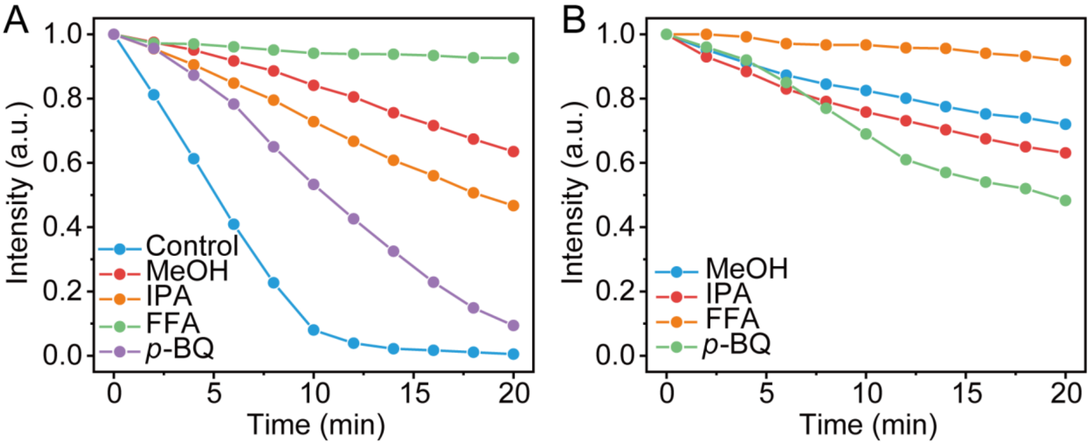

Figure S12. Effects of different quenchers on R6G removal performance in (A) CACNs/PMS and (B) Co_3O_4/PMS systems. Experimental conditions: $[R6G]_0$ = 10 mg L^{-1}, $[PMS]_0$ = 0.2 mM, $[catalyst]_0$ = 2 mg.

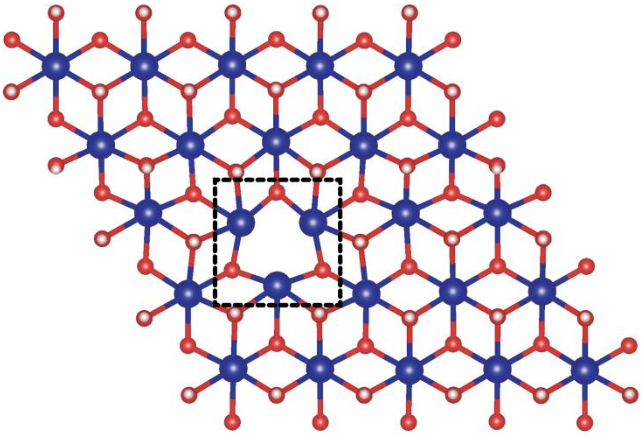

Figure S13. LDH model of $Co_5(O_{9.48}H_{8.52})NO_3$.

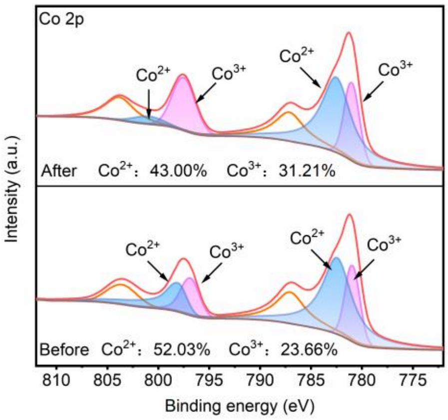

Figure S14. XPS spectra of Co 2p before and after catalytic reaction.

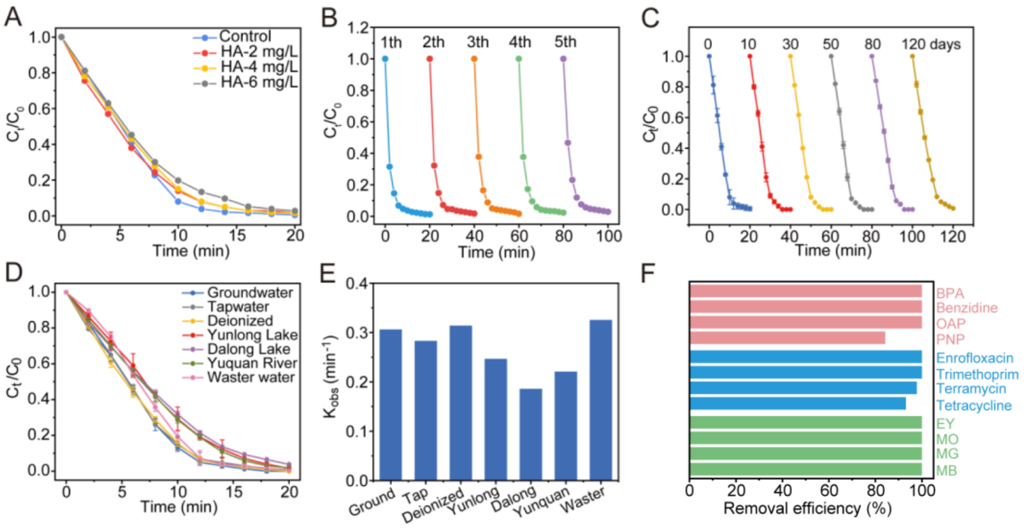

Figure S15. (A) Removal efficiency of R6G by CACNs under HA. (B) Five-cycle degradation performance of CACNs/PMS system. (C) Stability test of CACNs within 120 days. (D) Degradation performance and (E) the first-order rate constant of CACNs/PMS system for R6G in various water matrices. (F) Removal of multiple pollutants by CACNs activated PMS system. Experimental conditions: $[R6G]_0 = 10$ mg L^{-1}, [PMS] = 0.2 mM, [Catalyst] = 2 mg, T = 25 °C.

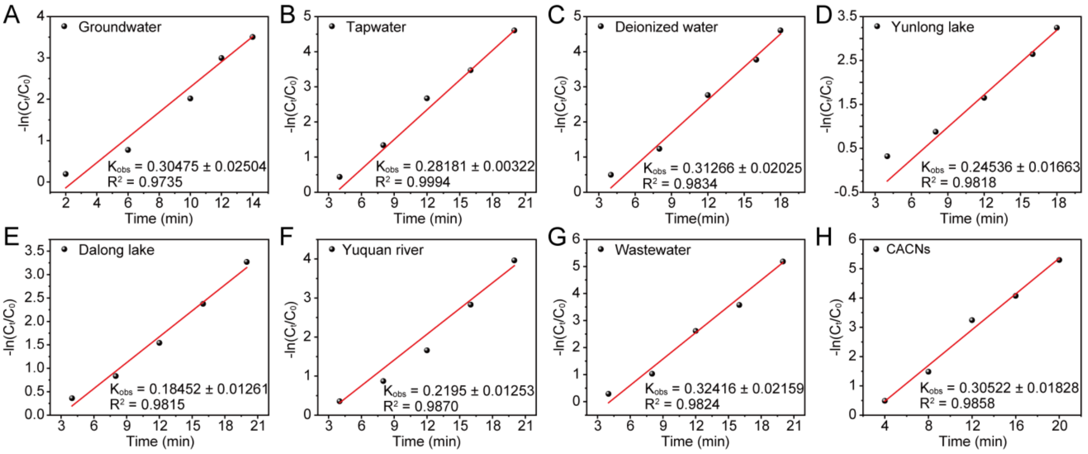

Figure S16. The first-order rate constants of R6G degradation catalyzed by CACNs/PMS system under different water quality.

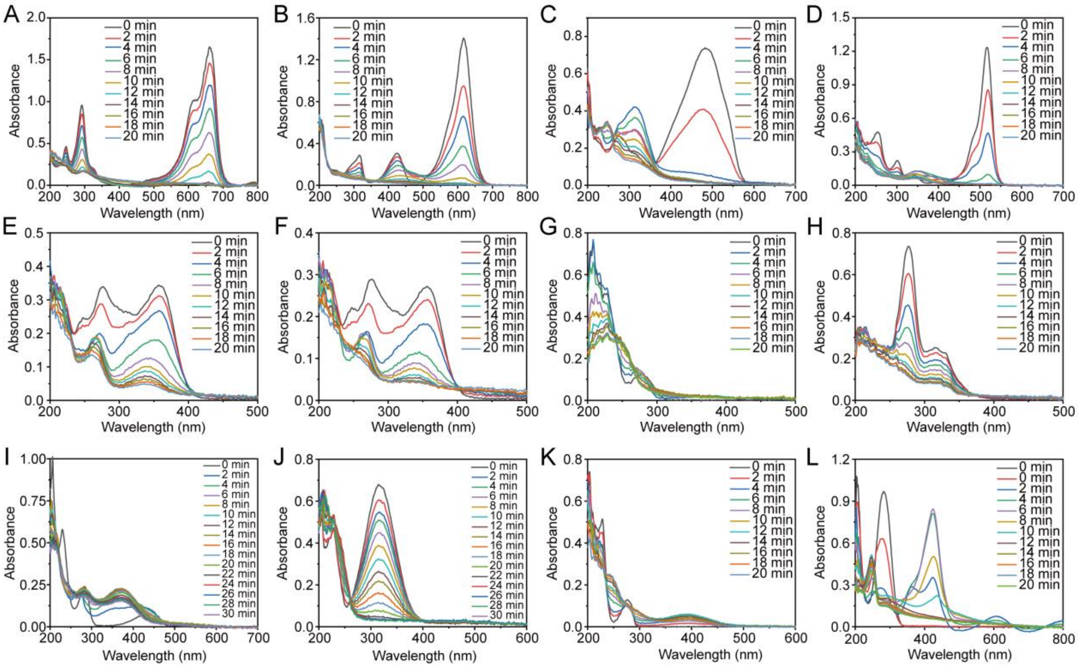

Figure S17. The time process of catalytic oxidation of different pollutants by PMS activated by CACNs.

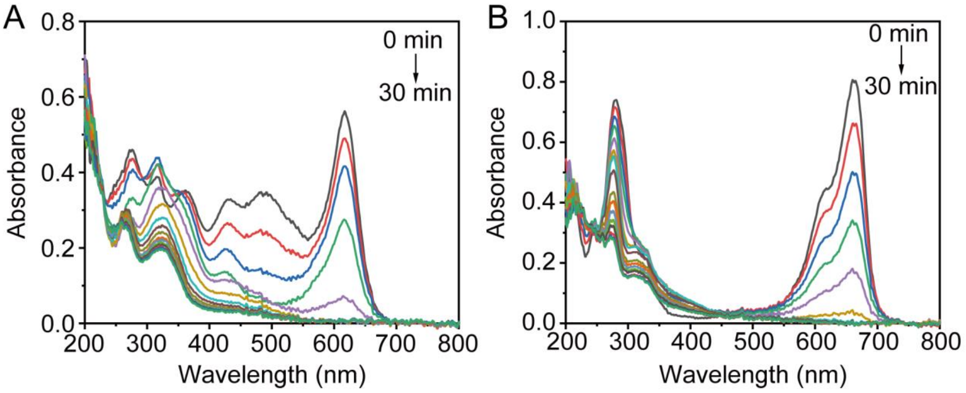

Figure S18. The time process of catalytic oxidation of various pollutants by PMS activated by CACNs in ultrapure water.

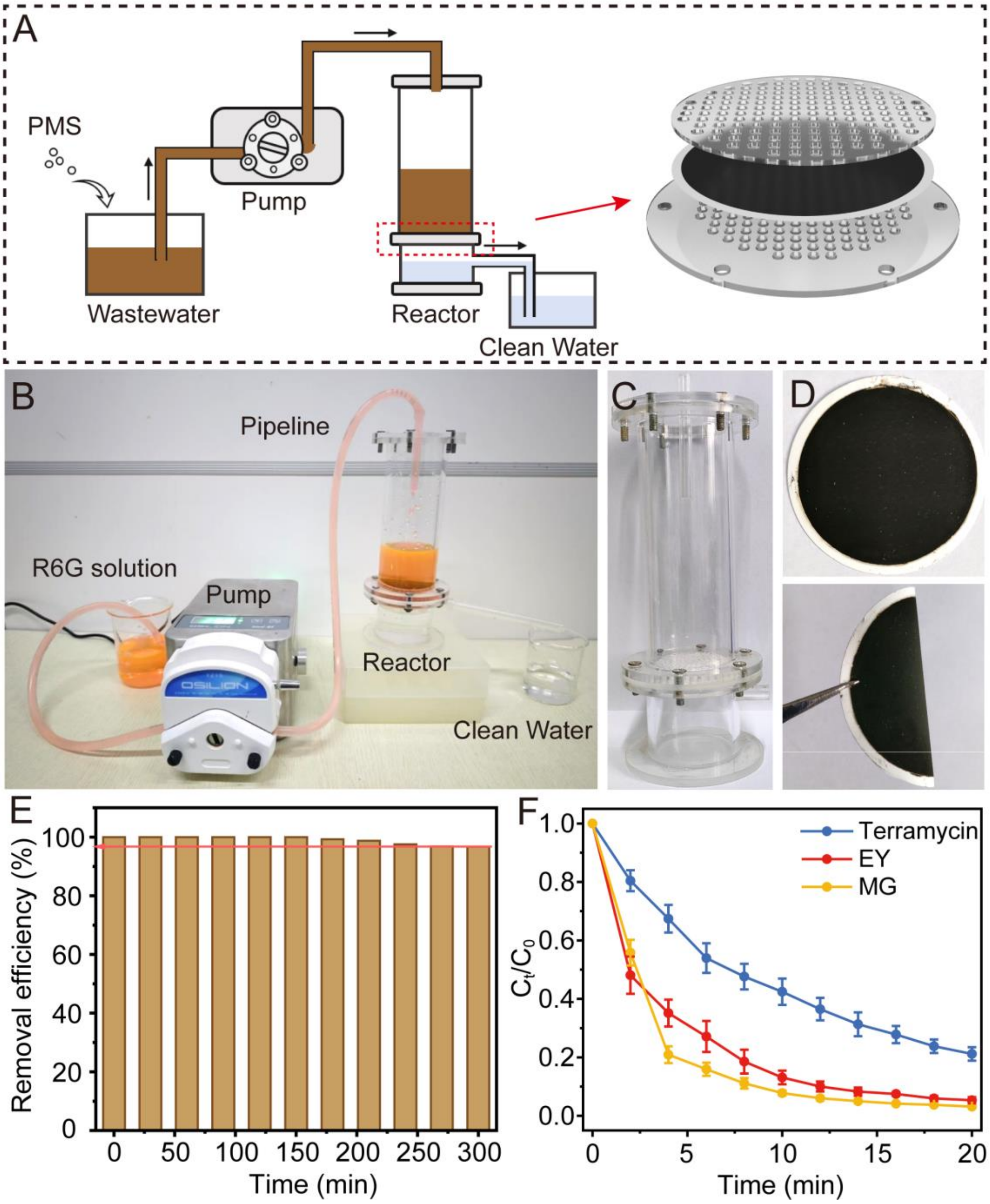

Figure S19. Micro-reactor design and performance of wastewater treatment. (A) Schematic illustration of wastewater treatment micro-reactor. (B) Structure diagram of catalytic reactor generating unit. (C) Photograph of the wastewater treatment micro-reactor and (D) the catalyst-loaded membrane. (E) Efficiency of the continuous flow catalytic process for removing R6G over a 300 min period. (F) The time process of catalytic oxidation of three pollutants by PMS activated by CACNs in industrial wastewater.

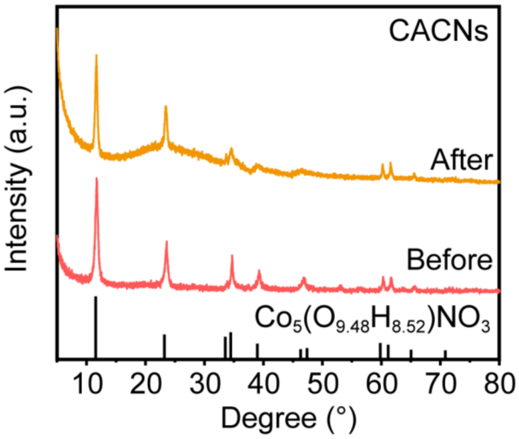

Figure S20. XRD of the CACNs on PVDF membrane.

Table S1: I_D/I_G values corresponding to Raman spectra of 15CACNs, 30CACNs and 50CACNs.

Sample	I_D/I_G
15CACNs	0.774
30CACNs	0.765
50CACNs	0.537

Table S2: BET surface area of 15CACNs, 30CACNs and 50CACNs.

Sample	Surface area (m^2 g^{-1})
15CACNs	111.798
30CACNs	89.894
50CACNs	63.123

Table S3: Metal element content in the samples.

Sample	Element	Content
30CACNs	Al	8.1%
	Co	38.8%
Solution after 5 degradation cycles	Al	220 μg L^{-1}
	Co	101 μg L^{-1}
Solution after continuous degradation for 300 min	Co	832 μg L^{-1}